Eur. Phys. J. E (2016) **39**: 36
DOI 10.1140/epje/i2016-16036-3

THE EUROPEAN PHYSICAL JOURNAL E

Regular Article

Collective dynamics of diffusiophoretic motors on a filament[⋆,⋆⋆]

Mu-Jie Huang[a] and Raymond Kapral[b]

Chemical Physics Theory Group, Department of Chemistry, University of Toronto, Toronto, Ontario M5S 3H6, Canada

Received 3 December 2015 and Received in final form 17 February 2016
Published online: 28 March 2016 –

Abstract. A variety of uses has been proposed for synthetic chemically powered nanomotors that exploit their autonomous directed motion. The collective dynamics of these and other active particles display features that differ from their equilibrium analogs. We investigate the collective dynamics of chemically powered diffusiophoretic motors attached to a filament. Rotational Brownian motion is reduced substantially when a motor is attached to a filament and this improves motor performance. When many motors are attached to the filament, structural and dynamical correlations that may extend over long distances arise. While some features of these correlations are due to packing on the filament, there are nonequilibrium effects that are due to the local concentration gradients of reactive species produced by all motors. As the motor density on the filament increases beyond a critical value, the average motor velocity projected along motor internuclear axis switches from forward to backward directions. Knowledge of the collective dynamics of motors on filaments should prove useful when designing ensembles of synthetic motors to perform tasks such as cargo transport involving delivery of material to specific regions in complex media.

1 Introduction

The collective behavior of active matter, where the constituent elements are either autonomous agents or are forced by external means, is very different from that of equilibrium systems. Active self-assembly, dynamic clustering, swarming, and giant number fluctuations are a few examples of phenomena observed in these systems. The mechanisms governing this diverse nonequilibrium behavior are currently under investigation and efforts are being made to elucidate the general principles that underlie the phenomena [1–3]. The active systems being studied are varied. They include, among others, birds, fish, microorganisms, forced granular particles and synthetic self-propelled motors. Reviews of active matter have been written that describe these phenomena and discuss the simulations and theoretical studies that have been carried out to help interpret the observed behavior [4–12].

Often studies of the collective dynamics of active systems are carried out for systems with two- or three-dimensional geometries. The collective dynamics in two-dimensional systems are easy to visualize and are relevant for many systems where the active motion takes place on substrates. The dynamics seen in three-dimensional systems is more varied. In the biological realm, particularly in the interior of a cell where molecular motors carry out numerous transport and other functions, molecular machines execute directed motion through conformational changes and walk on filaments [13, 14]. Usually, many motors of different kinds are attached to biomolecular filaments and they often act in a cooperative fashion to achieve their goals [15]. In this paper we explore some of the collective properties of synthetic motors that are attached to polymeric filaments. This investigation was prompted both by the fact that the directed motion of very small synthetic motors in bulk solution is strongly compromised by thermal fluctuations that give rise to rotational Brownian motion, and by potential applications that involve the dynamics of many such motors in complex geometries, or even in the cell.

In contrast to biological motors, many synthetic motors do not require conformational changes for their directed motion [16]. Studies of the dynamics of single motors and their collective behavior are topics of current research. For example, experimental studies of the active aggregation of Au-Pt Janus particles [17], self-assembly of Janus particles with hydrophobic hemispheres [18], and clustering in light-activated particle suspensions have been carried out [19–21]. Theoretical studies have indicated the presence of collective rotating structures in the absence of

⋆ Contribution to the Topical Issue "Nonequilibrium Collective Dynamics in Condensed and Biological Matter", edited by Holger Stark, Marcus Baer, Carsten Beta, Sabine Klapp and Andreas Knorr.

⋆⋆ Supplementary material in the form of three .mp4 files available from the Journal web page at
http://dx.doi.org/10.1140/epje/i2016-16036-3

[a] e-mail: mjhuang@chem.utoronto.ca
[b] e-mail: rkapral@chem.utoronto.ca

long-range particle velocity alignment [22,23], the importance of hydrodynamic interactions on collective phase behavior [24], the existence of orientational alignment among active particles [25], and the presence of diverse types of collective behavior of diffusiophoretically propelled Janus colloids [26].

The specific focus of this study is on synthetic motors that operate by chemically powered diffusiophoretic mechanisms [16,27,28]. In particular, we investigate the collective behavior of many such motors attached to a filament. The motor is modeled by a stiff chain composed of three linked beads. Chemical reactions that convert fuel into product take place on the surface of the catalytic bead in a motor, and the self-generated concentration gradients of reactive species gives rise to motor propulsion[1]. These motors are able to bind to a filament and we study their motions on the filament. We show that correlations of motor positions, orientations and velocities exist for sufficiently high motor concentrations. While the collective dynamics of active particles can arise from mechanisms that depend on effects such as local orientational alignment and hydrodynamic interactions, the collective dynamics of chemically powered motors is also strongly influenced by chemical concentration gradients. Many of the collective effects we find for motors on filaments can be traced to coupling through chemical concentration fields.

The outline of the paper is as follows. In sect. 2, we describe the model for the motor and filament, as well as the reactive mesoscopic method used to simulate the motor dynamics on a filament. The remaining sections present our investigations of how the concentration fields of reactive species and motor number affect the collective behavior. Section 3 shows some of the dynamical features of the velocities and orientations that are found as a function of motor density on the filament. Section 4 concerns steady-state correlations in the average positions, orientations and velocities, while sect. 5 deals with time correlations of collective motor dynamical variables. In these sections effects due to the local concentrations of reactive species arising from all motors are isolated by comparing results from motors that produce common- and distinct-product molecules. The conclusions of the paper are given in sect. 6.

2 System description

Coarse-grain models of both the motor and the filament on which it moves have been constructed as follows. The filament is a linear chain composed of beads (F). Neighboring beads in the chain are linked by harmonic springs, $V_{\rm bond} = \frac{1}{2}k_s(r-r_0^F)^2$, where k_s is the spring constant, and r_0^F is the equilibrium bond length. The bending stiffness of the filament is accounted for by a three-body potential, $V_{\rm bend} = k_b[1-\cos\theta]$, where k_b is the bending energy, and $\cos\theta = \hat{r}_{i-1,i}\cdot\hat{r}_{i,i+1}$, where $\hat{r}_{ij} = (\mathbf{r}_i - \mathbf{r}_j)/|\mathbf{r}_i - \mathbf{r}_j|$.

[1] The mechanism is similar to that for a sphere dimer motor. See [29].

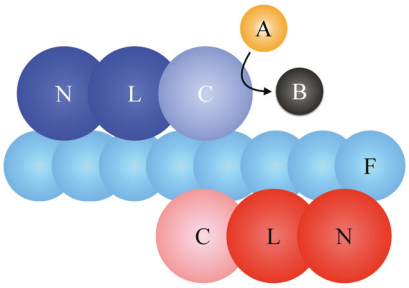

Fig. 1. Sketch of two chemically powered motors on the filament. Each motor consists of three beads: catalytic bead (C), neutral linker bead (L), and noncatalytic bead (N). The filament is a linear chain of beads (F). A catalytic reaction occurs when a fuel particle (A) encounters a C bead and is converted into a product particle (B). For future reference, motors are color coded by their orientation on the filament: a motor colored blue indicates that it is oriented so that the C head bead points to the right, whereas for motors colored red the head C bead points to the left. The catalytic beads in these motors are light blue and light red, respectively.

The motor is a short chain of three beads linked by harmonic springs with the same form as those for the filament but with equilibrium bond length r_0^M, while the bending stiffness is taken into account by adding a spring linking the end beads with an equilibrium bond length $2r_0^M$. The filament and the three-bead motor are similar to those of a three-bead oligomeric motor on a filament studied earlier [30] but the dynamical model is completely different. A chemical self-diffusiophoretic mechanism, where a reaction on a motor catalytic bead generates a concentration gradient that is felt by the other motor beads, is responsible for the directed motion of the motor. More specifically, each motor comprises catalytic (C) and noncatalytic (N) end beads linked by a neutral bead (L). The propulsion mechanism of this three-bead motor is similar to that of a sphere dimer motor [29] except that a neutral linker bead has been added in order to provide better control of the orientation of the motor when attached to the filament.

The motors and filament are contained in a rectangular box with dimensions $L_x = 40$ and $L_y = L_z = 20$ and periodic boundary conditions in all directions. The filament is oriented along the x-axis and is immobilized by applying an additional force to eliminate its center-of-mass translation [31]. The simulation volume also contains a number $N_S = N_A + N_B$ of A (fuel) and B (product) solvent particles. While solvent particles interact among themselves through multiparticle collisions [32–35], interactions with the motor and filament beads are taken into account by repulsive potentials $V_{\alpha S}(r_{ij})$ with strength $\epsilon_{\alpha S}$, where $r_{ij} = |\mathbf{r}_i - \mathbf{r}_j|$ is the separation of particle i of type α from particle j of type S, and $\alpha = C, L, N, F$ and $S = A, B$ (see appendix A for details).

A schematic picture showing motors attached to the filament is given in fig. 1. A concentration gradient is generated by an irreversible chemical reaction, $C+A \rightarrow C+B$ that occurs with unit probability when a fuel particle encounters the C bead on a motor, converting a fuel A par-

Table 1. The average number of motors attached to the filament, $N_{\rm on}$, the average line density of motors attached to the filament, $n_{\rm mf} = N_{\rm on}/L_x$, the average time that a motor remains attached to the filament $t_{\rm on}$ ($\times 10^5$) and the fraction of the total simulation time $t_{\rm sim} = 5 \times 10^5$ that a motor remains attached, $f_{t_{\rm on}} = t_{\rm on}/t_{\rm sim}$, for various values of the number of motors in the system, $N_{\rm m}$, whose corresponding average density is $n_{\rm m} = N_{\rm m}/V$ ($\times 10^4$). $N'_{\rm on}$ is the number of motors that are attached to the filament for the entire simulation length.

$N_{\rm m}$	4	6	8	10	12	14	16
$n_{\rm m}$	2.50	3.75	5.00	6.25	7.50	8.75	10.0
$N_{\rm on}$	3.99	5.99	7.96	9.96	11.88	13.26	13.63
$n_{\rm mf}$	0.10	0.15	0.20	0.25	0.30	0.33	0.34
$t_{\rm on}$	4.9	4.9	4.4	4.5	3.96	2.11	1.23
$f_{t_{\rm on}}$	0.98	0.98	0.88	0.90	0.79	0.42	0.25
$N'_{\rm on}$	3.98	5.94	6.38	9.06	10.02	7.5	6.2

ticle into a product B particle. The interactions of the product B species with the noncatalytic end beads have $\epsilon_{NB} = 0.1\,\epsilon$ interaction strengths, while $\epsilon_{CA} = \epsilon_{CB} = \epsilon_{LA} = \epsilon_{LB} = \epsilon_{NA} = \epsilon$. For these interaction parameters an individual motor in solution will move in a direction with the C bead at its head. In order to maintain the system in a nonequilibrium steady state the reaction $B \rightarrow A$, that removes product B and replenishes fuel A is carried out in the bulk of the solution. The reactive version of multiparticle collision dynamics is used to effect these reactions [36]. Additional details concerning the algorithm and system parameters are given in appendix A.

3 Motor orientation and velocity

When a filament is present in the system motors tend to bind to it as a result of solvent depletion forces. Once bound, thermal fluctuations may cause motors to detach but they remain attached for long periods of time. When motors are attached to a filament one expects that orientational Brownian motion will be partially suppressed leading to longer reorientation times. In such a case the time domain over which ballistic motion induced by self-propulsion persists will be longer and the resulting enhanced directed motion could be exploited in applications.

The orientational relaxation time τ_R can be computed from the decay of the time-dependent orientational correlation function, $C_u(t) = \langle \hat{\mathbf{u}}(t) \cdot \hat{\mathbf{u}}(0) \rangle$. Here $\hat{\mathbf{u}}(t) = (\mathbf{R}_C(t) - \mathbf{R}_N(t))/|\mathbf{R}_C(t) - \mathbf{R}_N(t)|$ is a unit vector along the internuclear axis from the N bead to the C bead in the motor. This relaxation time is in fact greatly increased for motors attached to filaments. We find $\tau_R \approx 245$ for a motor in solution, which is about 425 times shorter than $\tau_R \approx 104\,000$ when the motor is attached to the filament.

The line density of motors on the filament, defined as the average number of motors attached to the filament per unit length of filament, $n_{\rm mf} = N_{\rm on}/L_{\rm f}$, where $L_{\rm f} = L_x$ is the filament length, is an important quantity that determines the nature of the collective behavior. In particular, as $n_{\rm mf}$ increases, so do the interactions among motors. Such interactions can cause motors to detach more frequently and lead to coupling among motors mediated by species concentration fields. Table 1 lists the number of motors ($N_{\rm m}$) in the system with volume V and the corresponding motor density in the system ($n_{\rm m} = N_{\rm m}/V$), the average number of motors attached to the filament ($N_{\rm on}$) and the corresponding motor line density ($n_{\rm mf}$), the average length of time a motor is attached to the filament ($t_{\rm on}$), and the fraction of the total simulation time ($f_{t_{\rm on}}$) that a motor is attached to the filament. For small $n_{\rm mf} < 0.25$, $t_{\rm on}$ is comparable to the total simulation time $t_{\rm sim} = 5 \times 10^5$ and $n_{\rm mf}$ steadily increases. For $n_{\rm mf} > 0.25$, $n_{\rm mf}$ rapidly reaches a saturation value and $f_{t_{\rm on}}$ steadily decreases. To confirm that these results are robust and are not significantly affected by the periodic boundary conditions, simulations with $L_x = 80$ and $N_{\rm m} = 28$ ($n_{\rm m} = 8.75 \times 10^{-4}$) were performed. The results show that $n_{\rm mf} = 0.32$, comparable to that in table 1 for the smaller system size.

Since the filament lies along the x-axis and is nonpolar, a motor attached to it can move in the $+\hat{x}$ or $-\hat{x}$ directions, giving rise to a quasi-one-dimensional trajectory along the x-axis. This trajectory may be monitored by observing the x-component of the L bead position, $R_x(t) = \mathbf{R}_L(t) \cdot \hat{\mathbf{x}}$; the motor orientation may be described by $u_x(t) = \hat{\mathbf{u}}(t) \cdot \hat{\mathbf{x}}$.

Figure 2(a) shows the trajectories of a system with motor line density $n_{\rm mf} = 0.1$. The correlation between the direction of motor movement and its orientation can be seen by considering one of these motors indicated in red. The orientation $u_x(t)$ of this motor is plotted in panel (b). Starting from an initial position near $R_x = 0$, one can see that the motion of this motor in a given direction along the filament is strongly correlated with its orientation in that direction. This correlation persists for long periods of time. For example, at time $t \approx 3 \times 10^5$ the motor rapidly flips its orientation from $u_x \sim -1$ to $u_x \sim +1$, and consequently the motor switches its propagation direction from $-\hat{x}$ to $+\hat{x}$. This is the behavior that one would expect for a single motor or an ensemble of independent motors.

This is no longer the case when the motor line density is larger. Referring to data in fig. 2 for $n_{\rm mf} = 0.33$, in the time interval $10^5 < t < 3 \times 10^5$ one can see that the motor moves in the $+\hat{x}$ direction, which is opposite to its orientation. By contrast, for $n_{\rm mf} = 0.25$ there is no pronounced directed motion.

The change in character of motor dynamics with motor line density $n_{\rm mf}$ can be seen clearly in the variation of the average of the motor velocity projected on its orientation,

$$\langle V_u \rangle = \left\langle \frac{1}{N_{\rm on}} \sum_{i=1}^{N_{\rm on}} \mathbf{V}_i(t) \cdot \hat{\mathbf{u}}_i(t) \right\rangle, \qquad (1)$$

where the angle brackets denote a time average and ensemble average over 50 realizations of the dynamics. The velocity of motor i is computed as $\mathbf{V}_i(t) = (\mathbf{R}_i(t + \Delta t) - \mathbf{R}_i(t))/\Delta t$ with $\Delta t = 5000$. Figure 3 shows $\langle V_u \rangle$ as a function of $n_{\rm mf}$ (black circles). While $\langle V_u \rangle > 0$ for $n_{\rm mf} < 0.25$,

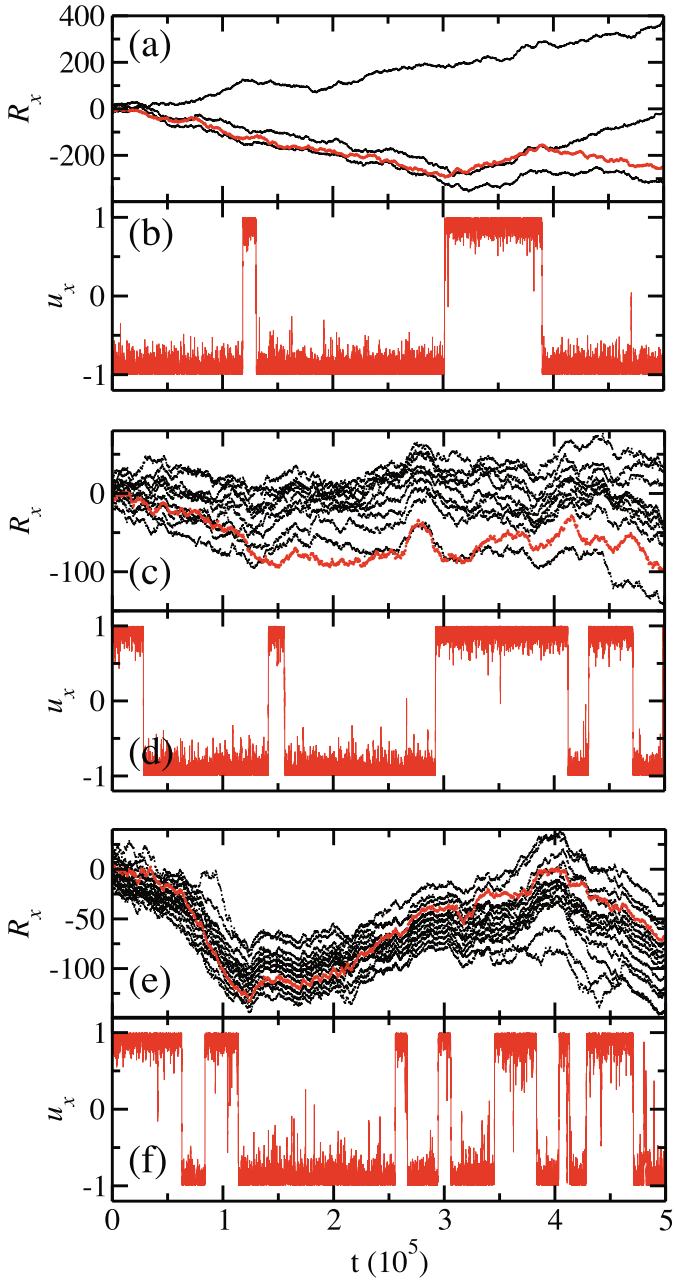

Fig. 2. Motor trajectories $R_x(t)$ for different numbers of motors on the filament: (a) $N_m = 4$, (c) $N_m = 10$ and (e) $N_m = 14$ motors. The orientation (u_x) of the motors indicated by the red trajectories in panels (a), (c) and (e) are plotted in panels (b), (d) and (f), respectively. Videos of the simulations for panels (a), (c) and (e) are available in the Supplementary Material. The motors indicated by red trajectories are labeled by black arrows in the video.

it is negative for $n_{mf} > 0.25$ so that $n_c \approx 0.25$ is the critical motor line density beyond which the motors, on average, start to move in a direction opposite to that of their natural propagation direction when isolated. For sufficiently high motor line densities interactions among many motors lead to a change in the character of the average motor velocity. (Backward motions were also observed when

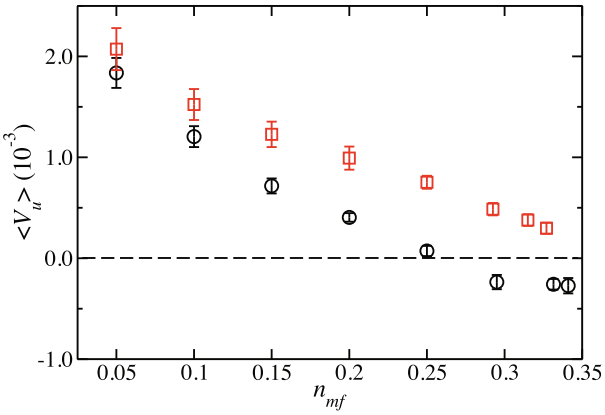

Fig. 3. The average value of the projection of the velocity of a motor along its internuclear axis, $\langle V_u \rangle$, as a function of the motor line density, n_{mf}, for common-product molecules (black circles) and distinct-product molecules (red circles). The dashed line indicates zero mean velocity.

the filament length and N_m were doubled for $n_{mf} > 0.25$, which indicates that these results do not depend significantly on system size.)

The system contains N_m identical motors and each motor converts fuel A to product B, a product common to all motors. We now show that it is the effect of the net B concentration field that gives rise to the correlations discussed above. To examine this effect we consider a similar ensemble of N_m motors but now each motor i produces a distinct product B_i, so that only the self-generated concentration gradient of B_i is responsible for the propulsion of that motor. The values of $\langle V_u \rangle$ for motors producing distinct-product molecules are plotted in fig. 3 as a function of n_{mf} (red squares). Now $\langle V_u \rangle > 0$ for all n_{mf}.

The change in character of the average number density field of B product particles, n_B, in the vicinity of a motor attached to the filament is shown in fig. 4. This figure plots $n_B(n_1, n_2)$ as a function of two in-plane coordinates (n_1, n_2). (A detailed description of how the concentration field was determined in given in appendix B.) For $n_{mf} = 0.1$, the density field is higher at the interface between the L and N beads than at the rear surface of the N bead. Therefore, a motor is expected to move forward in the same direction as its orientation. While the $n_B(n_1, n_2)$ density is negligible at the rear surface of the noncatalytic bead for $n_{mf} = 0.1$, it increases with increasing n_{mf}. When $n_{mf} = 0.33$ the $n_B(n_1, n_2)$ density at this location is somewhat higher than that at the N-L interface. Consequently, the product concentration gradient across the noncatalytic bead for $n_{mf} = 0.33$ is in a direction opposite to that for $n_{mf} = 0.1$, indicating motion opposite to its orientation. For $n_{mf} = 0.25$ the concentration fields at these locations become comparable and a less strong propulsion is expected and found.

To confirm the redistribution of product particles in the vicinity of the N bead, the angular dependence of the average product concentration field in the interaction zone of the N bead, $\langle n_B \rangle$, was computed and is shown in fig. 5. The angle θ is defined as $\theta = \cos^{-1}(\hat{\mathbf{u}} \cdot \mathbf{r}/|r|)$,

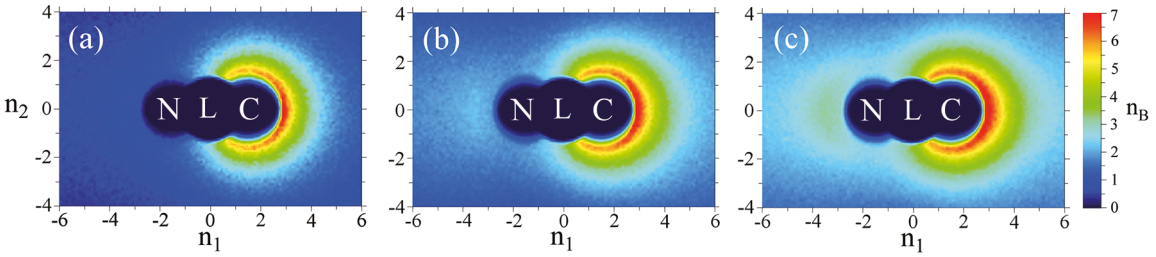

Fig. 4. The average number density field of B product particles in the vicinity of the motor, $n_B(n_1, n_2)$, for (a) $n_{\rm mf} = 0.1$, (b) $n_{\rm mf} = 0.25$ and (c) $n_{\rm mf} = 0.33$.

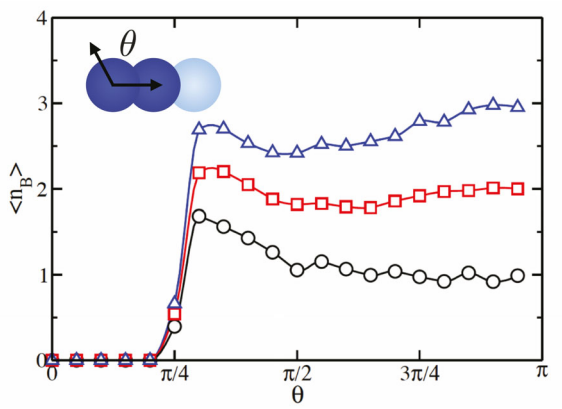

Fig. 5. The angular distribution of the average number of B product particles in the interaction zone of the N bead for $n_{\rm mf} = 0.1$ (black circles), 0.25 (red squares) and 0.33 (blue triangles).

where $\mathbf{r}$ is the position of a B particle relative to the N motor bead; therefore, $\theta \approx \pi/4$ and $\theta = \pi$ correspond to the front (N-L interface) and the rear surface of the N bead, respectively. Only the particles located in the interaction zone are taken into account, *i.e.*, the condition $\sigma_{NS} < |r| < 2^{1/6}\sigma_{NS}$ must be satisfied, where $\sigma_{NS} = (d_N + d_S)/2$ is the sum of the radii of N and S particles. For $n_{\rm mf} = 0.1$, the maximum of $\langle n_B \rangle$ lies near $\theta \approx \pi/4$, indicating forward motor motion. However, when $n_{\rm mf} = 0.33$, $\langle n_B \rangle$ is largest when $\theta \approx \pi$ indicating a switch of motor propagation direction. As might be anticipated, for $n_{\rm mf} = 0.25$, the motor does not exhibit directed motion as a result of the approximately flat angular distribution of $\langle n_B \rangle$.

4 Correlations in motor positions, orientations and velocities

Steady-state correlations of the motor positions, orientations and velocities develop when many motors are attached to the filament. Positional correlations can be probed by examining the L-L radial distribution function,

$$g(x) = \left\langle \frac{L_{\rm f}}{N_{\rm on}^2} \sum_{j<i=1}^{N_{\rm on}} \delta\left(|R_{L,xi} - R_{L,xj}| - x\right) \right\rangle, \qquad (2)$$

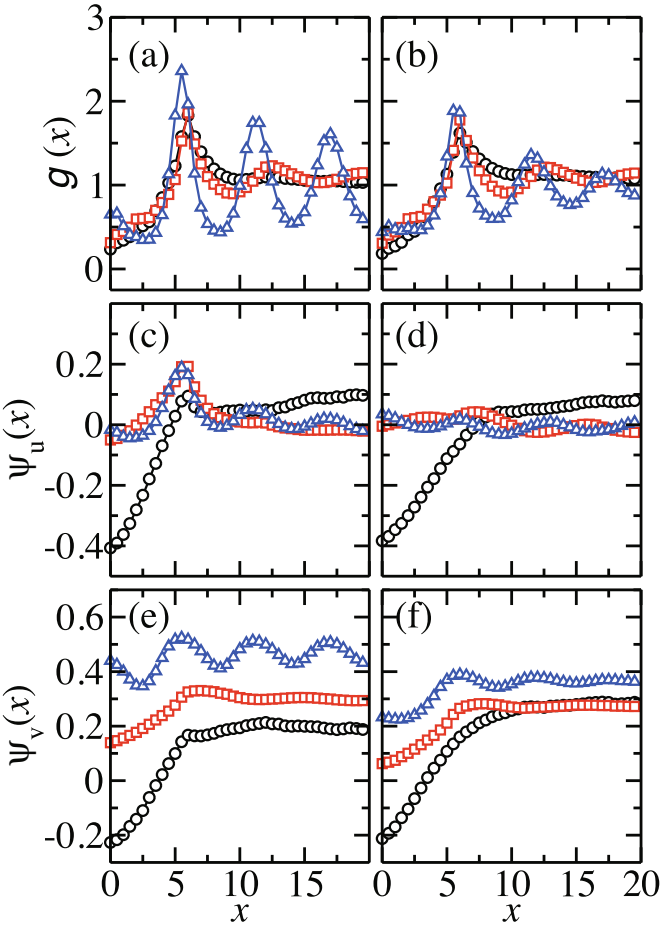

Fig. 6. The radial distribution function $g(x)$, the spatial correlation functions of orientational ordering $\psi_\phi(x)$ and velocity $\psi_v(x)$ for common-product simulations are shown in (a), (c) and (e), and distinct-product simulations in (b), (d) and (f), respectively. Results for $n_{\rm m} = 0.1$, $n_{\rm m} = 0.25$ and $n_{\rm m} = 0.33$ motors are shown as black circles, red squares and blue triangles, respectively.

where $R_{L,xi}$ is the x-component of the position of bead L of motor i and $L_{\rm f}$ is the filament length. The bracket again signifies an average over time and realizations. (For notational convenience we have not explicitly indicated the time dependence of the variables in the average.) Figure 6 plots $g(x)$ for $n_{\rm mf} = 0.1$ (black circles), 0.25 (red squares) and 0.33 (blue triangles). There is a well-defined

peak at $x \simeq 6$ for $n_{\rm mf} = 0.1$ and 0.25, which shifts to somewhat smaller values for $n_{\rm mf} = 0.33$. This peak corresponds to the average distance between two neighboring motors. The radial distribution function for $n_{\rm mf} = 0.33$ shows the presence of long-range order. It has several peaks that extend to $x \approx 17.5$, half the size of the simulation box. Figure 7 shows motor configurations on the filament for several values of $n_{\rm mf}$. The signatures of long-range order for $n_{\rm mf} = 0.33$ can be seen in this single configuration.

Local orientational ordering along filament can be described by the orientation correlation function

$$\psi_u(x) = \left\langle \frac{1}{n(x)} \sum_{j<i=1}^{N_{\rm on}} u_{xi} u_{xj} \delta\left(|R_{L,xi} - R_{L,xj}| - x\right) \right\rangle, \tag{3}$$

where u_{xi} is the x-component of the unit vector specifying the orientation of motor i, $n(x) = \sum_{j<i=1}^{N_{\rm on}} \delta(|R_{L,xi} - R_{L,xj}| - x)$ is the number of motor pairs separated by the distance x. Using this definition, two motors separated by the distance x have the same or opposite orientations when $\psi_u(x) > 0$ or $\psi_u(x) < 0$, respectively, whereas $\psi_u(x) = 0$ indicates that there is no preferential orientation for the two motors in the pair. In fig. 6 we see that for small motor density ($n_{\rm mf} = 0.1$, black circles), negative values of $\psi_u(x)$ are found for small separations since motors with opposite orientation have a higher probability to encounter each other. There is a peak at $x \simeq 6$, which, in conjunction with the maximum found in $g(x)$ at the same x, suggests that two neighboring motors tend to align. The function $\psi_u(x)$ takes positive values for large x at low motor densities on the filament since, for low densities, motors with similar alignment will propagate in the same direction with only rare encounters. Figure 7 shows an instantaneous configuration for $n_{\rm mf} = 0.1$ where several motors propagate in the same direction. As the motor density increases to $n_{\rm mf} = 0.24$, the peak at $x \simeq 6$ sharpens. In addition, $\psi_u(x)$ vanishes at $x = 1$ and $x = 20$ because the frequency of motor reorientations increases with an increase in $n_{\rm mf}$. An instantaneous configuration for this motor number is also shown in fig. 7. For $n_{\rm mf} = 0.33$, which is larger than the critical number $n_{\rm c}$, additional peaks are found in $\psi_u(x)$ at the same positions as the maxima of $g(x)$, signaling the development of long-range orientational order.

Local directional ordering is described by the local velocity correlation function,

$$\psi_v(x) = \left\langle \frac{1}{n(x)} \sum_{j<i=1}^{N_{\rm on}} v_{xi} v_{xj} \delta\left(|R_{L,xi} - R_{L,xj}| - x\right) \right\rangle, \tag{4}$$

where $v_{xi} = \hat{\mathbf{x}} \cdot \mathbf{V}_i / |\mathbf{V}_i|$ is the x-component of the normalized velocity of motor i. This function measures the degree of correlation of directed motion between two motors separated by a distance x. The positive (negative) values of $\psi_v(x)$ indicate whether two motors are moving in the same (opposite) velocity directions, whereas $\psi_v(x) = 0$ indicates no correlation in the directed motion of two motors on the filament. For $n_{\rm m} = 0.1$ we saw that the orientations of two motors are antiparallel at short distances and parallel at long distances. Also, on average, the velocity of a motor projected onto its orientation is positive for small $n_{\rm mf}$. Consequently, one expects and finds in fig. 6 negative and positive values of $\psi_v(x)$ at short and long distances, respectively, for small $n_{\rm mf}$. As $n_{\rm mf}$ increases to $n_{\rm mf} = 0.25$, $\psi_v(x)$ takes positive values for all x indicating collective motor motion on the filament. This collective motion for $n_{\rm mf} = 0.25$ can be seen in the motor trajectories in fig. 2; for example, in the time interval $2.5\times10^5 < t < 3\times10^5$, the motors move as a transient cluster toward $+\hat{x}$ followed by motion in the reverse direction. When the motor number further increases to $n_{\rm mf} = 0.33$, enhanced directional ordering is observed that gives rise to the coherently moving motor trajectories shown in this figure.

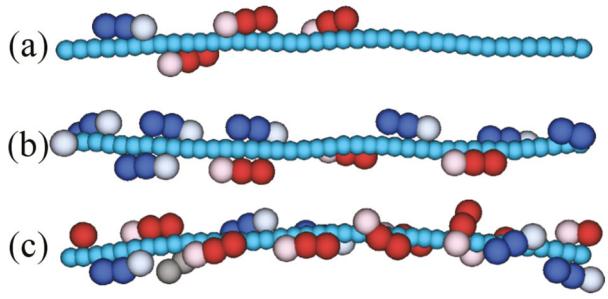

Fig. 7. Instantaneous configurations of motors on the filament drawn from the trajectories in fig. 2: (a) $n_{\rm mf} = 0.1$ at $t = 3 \times 10^5$, (b) $n_{\rm mf} = 0.25$ at $t = 3 \times 10^5$, and (c) $n_{\rm mf} = 0.33$ at $t = 2.5 \times 10^5$. The gray beads shown in panel (c) belong to the motor that detaches from the filament.

One may ask if the correlations described above arise simply from packing on the filament or have important contributions due to other sources. We examine effects arising from the local product concentration field by again comparing the results described above with those for motors that produce distinct products.

The same correlation functions for distinct-product motors are also plotted in fig. 6. The radial distribution functions for $n_{\rm mf} = 0.1$ and 0.25 are similar to those for motors that produce common products; however, for $n_{\rm mf} = 0.33$ the long-range correlations decay more rapidly. There is negligible orientational ordering for $n_{\rm mf} = 0.25$ and 0.33 for distinct products (note the absence of a strong peak at $x \approx 6$ that arises from the alignment of active neighboring motors). Correlations in directional ordering are substantially reduced for distinct-product motors.

These results suggest that for $n_{\rm mf} > n_{\rm c}$ correlations in $g(x)$ are largely due motor crowding on the filament but the structure is affected by the local product concentration field. Orientational order seen in $\psi_u(x)$ is substantially smaller for distinct-product motors. The long-range orientational order that is observed for motors producing common products indicates that configurations where the rear N bead of one motor and the front C bead of a neighboring motor are adjacent occur with high probability. In

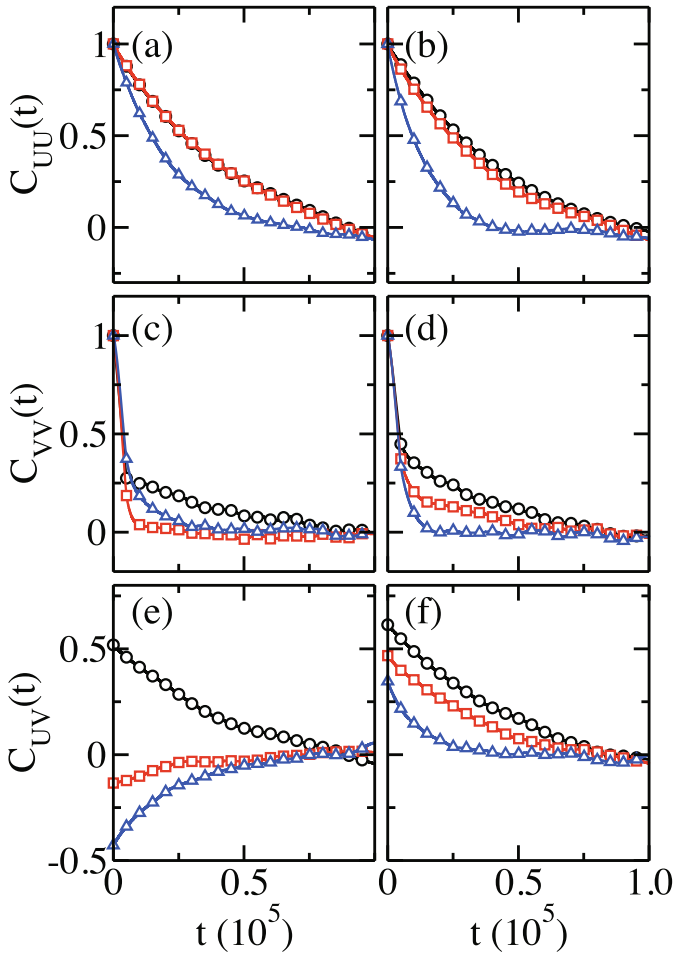

Fig. 8. Autocorrelation functions of system orientational $C_{UU}(t)$, velocity $C_{VV}(t)$ and orientation-velocity cross-correlation function $C_{UV}(t)$. Results for common-product simulations are shown in (a), (c) and (e), and distinct-product simulations in (b), (d) and (f), for $n_{\rm mf} = 0.1$ (black circles), $n_{\rm mf} = 0.25$ (red squares) and $n_{\rm mf} = 0.33$ (blue triangles).

such a packed alignment, the number of product particles in the vicinity of the N beads increases.

5 Collective dynamical properties

The dynamics of the collective behavior can be characterized by time correlations of various motor variables. These correlations take the general form

$$C_{FG}(t) = \frac{\langle (F(t) - \bar{F})(G(0) - \bar{G}) \rangle}{\sigma_F \sigma_G}, \qquad (5)$$

where $F(t)$ and $G(t)$ are collective motor variables with means $\bar{F}$ and $\bar{G}$, and standard deviations σ_F and σ_G, respectively. Results will be presented for motors that produce both common and distinct products in order to further assess coupling that has its origin in the product concentration field.

The instantaneous mean orientation is defined as

$$U(t) = \frac{1}{N_{\rm on}} \sum_{i=1}^{N_{\rm on}} u_{xi}(t). \qquad (6)$$

Figure 8 shows $C_{UU}(t)$ for common- and distinct-product motors with $n_{\rm mf} = 0.1$ (black circles), 0.25 (red squares) and 0.33 (blue triangles), respectively. The correlation functions for $n_{\rm mf} = 0.1$ and 0.25 are similar for both kinds of motor. This suggests that when $n_{\rm mf} < n_{\rm c}$ the motor reorientation rate has only a weak dependence on the interactions mediated by the product concentration field. For $n_{\rm mf} = 0.33$, $C_{UU}(t)$ decreases more slowly for common products. This can be attributed to the enhanced long-range orientational ordering along the filament seen in $\psi_u(x)$.

The instantaneous mean velocity projected on the filament direction is defined as

$$V(t) = \frac{1}{N_{\rm on}} \sum_{i=1}^{N_{\rm on}} v_{xi}(t). \qquad (7)$$

For $n_{\rm mf} = 0.1$ and 0.33 one can see in the figure that $C_{VV}(t)$ decays rapidly for $t < 10^4$, followed by a slow decay for later times; however, for $n_{\rm mf} = 0.25$ this correlation function decays rapidly to zero without exhibiting a significant long-time decay region. As discussed earlier, for this value of $n_{\rm mf}$ the concentration field is such that the average velocity of a motor is near zero. The figure shows that the decay is less rapid at long times for distinct products, since in this case the motors will move with nonzero mean velocity.

The cross correlation between these two collective variables, $C_{UV}(t)$, most clearly reflects the importance of the effects mediated by product concentration. This function measures the time correlation of the system velocity projected on the system orientation, and positive (negative) values of $C_{UV}(t)$ indicate forward (backward) collective motion. Note the significant differences between these correlation functions for common- and distinct-product simulations shown in fig. 8. For common-product motors a switch from forward to backward collective motion was found when $n_{\rm mf}$ was larger than the critical motor density $n_{\rm c}$, while no significant changes in collective directed motion were seen for distinct-product motors. Based on these observations, backward motions are again evidently caused by product-mediated interactions.

Finally, to investigate motor behavior on different time scales, the mean square displacement

$$\mathrm{MSD}(t) = \left\langle \frac{1}{N'_{\rm on}} \sum_{i}^{N'_{\rm on}} |R_{x,i}(t) - R_{x,i}(0)|^2 \right\rangle \qquad (8)$$

was computed. Only the trajectories of the $N'_{\rm on}$ motors that are attached to the filament for the entire simulation length were taken into account in the calculation of MSD(t) plotted in fig. 9. In the course of the dynamics motors can attach and detach from the filament as described above. From table 1 we see that the fraction of

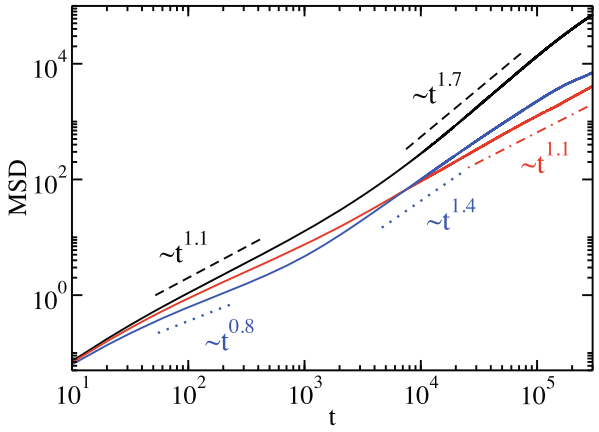

Fig. 9. Log-log plot of the mean square displacement (MSD) for common-product simulations for $n_{\rm mf} = 0.1$ (black solid line), $n_{\rm m} = 0.25$ (red solid line) and $n_{\rm mf} = 0.33$ (blue solid line). Fits to the MSD are indicated by black dashed lines for $n_{\rm mf} = 0.1$, red dash-dot lines for $n_{\rm m} = 0.25$ and blue dotted lines for $n_{\rm mf} = 0.33$.

time a motor remains attached to the filament varies between approximately unity at small motor line densities to 0.25 at the highest line density. Correspondingly, the fraction of the number of motors that remain attached for the entire simulation time, $N'_{\rm on}/N_{\rm on}$, varies between unity and 0.45 as the density increases. Consequently, since the time scale over which the diffusive motion was monitored was taken to be approximately equal to the shortest average time a motor remains attached to the filament, the MSD defined above will capture both short- and long-time features of the diffusive motion on the filament. The results show a transition from short-time diffusive motion to long-time super-diffusive motion for $n_{\rm mf} = 0.1$ (black circles) and 0.33 (blue triangles) at $t \approx 10^3$–10^4, while for $n_{\rm mf} = 0.25$ (red squares) diffusive motion is seen at both short and long times. These MSD data are consistent with observed the short- and long-time behavior of $C_{VV}(t)$. The long-time superdiffusive dynamics indicates that the directed motion on the filament plays an important role since the reorientation time is comparable to the simulation duration.

The diffusive motion of the motors for $n_{\rm m} = 0.25$ is again due to the fact that the product densities at the rear surface of the N bead and at the N-L interface are comparable. In this case there is no net directed force acting on the motors, and this results in diffusive dynamics for both short and long times.

6 Conclusion

This investigation of diffusiophoretic motors on filaments showed that both the structural and dynamical collective properties of many attached motors depend on their active character and the mechanisms giving rise to this activity. When the line density of attached motors is high, positional and orientational order has long-range correlations, which is not due solely to simple packing effects. Instead, various features of the correlations can be traced to interactions among the motors mediated by chemical species concentration gradients. This is a collective response of the motors to the concentrations of reactive species produced by all motors, in contrast to the response of a single motor to its self-generated concentration gradient that leads to its propulsion. In addition to correlations between the propagation direction of a motor and its orientation, there are regimes where the mean velocity of a motor in the ensemble points in a direction opposite to that it would have when isolated. This backward motion occurs when the number of motors on the filament exceeds a critical density $n_{\rm mf} = n_{\rm c}$. These effects are mediated by the local concentration field generated by different motors on the filament and were confirmed by simulations in which each motor responds to the concentration field generated only by its own catalytic activity.

Part of the stimulus for this study is the observation that biological molecular machines typically move along biofilaments in order to carry out their functions, such as cargo transport to specific locations. Synthetic chemically powered motors that utilize phoretic mechanisms for their propulsion can follow chemical gradients but are subject to strong orientational Brownian motion that quickly turns their ballistic motion into enhanced diffusion. By utilizing filaments in a fashion analogous to that of biological motors, not only can orientational Brownian motion be strongly suppressed, but motor motion can be targeted to specific locations. However, in contrast to most biological molecular motors where motion is biased in a particular direction, the motors and filaments in this study were nonpolar so that motion is equally likely in either direction on the filament. Thus, it could be interesting and useful to design motors or filaments that introduce such a bias in the motion. For example, as demonstrated in our previous study [30], one can make a motor so that one of its end beads is able to catalytically convert a filament bead into a new form. Then, by introducing different binding affinities of the motor beads with the filament, biased motion on the filament can be obtained. The motor and filament system in this study is only one of many possibilities that can be constructed to enhance directed motion of diffusiophoretic motors in complex media.

This work was supported by a grant from the Natural Sciences and Engineering Research Council of Canada. Computations were performed on the GPC supercomputer at the SciNet HPC Consortium. SciNet is funded by: the Canada Foundation for Innovation under the auspices of Compute Canada; the Government of Ontario; Ontario Research Fund - Research Excellence; and the University of Toronto [37].

Appendix A. Simulation method and parameters

The motors and filament are contained in a $40\,\sigma \times 20\,\sigma \times 20\,\sigma$ box. Each filament bead has diameter $d_F = 1.5\,\sigma$, while the diameters of the motor beads are $d_C =$

$d_L = d_N = 2\sigma$. The motors interact with the filament through attractive solvent depletion potentials plus repulsive Lennard-Jones (LJ) potentials, $V_{\alpha\alpha'}(r_{ij}) = 4\epsilon_{\alpha\alpha'}[(\sigma_{\alpha\alpha'}/r_{ij})^{12} - (\sigma_{\alpha\alpha'}/r_{ij})^6 + 1/4]\Theta(r_c - r)$, where $\Theta(r)$ is the Heaviside function, and the separation of particle i of type α from particle j of type α' is $r_{ij} = |\mathbf{r}_i - \mathbf{r}_j|$, where $\alpha, \alpha' \in \{C, L, N, F\}$. The interaction strength is $\epsilon_{\alpha\alpha'}$ when the separation $r_{ij} < r_c = 2^{1/6}\sigma_{\alpha\alpha'}$, with $\sigma_{\alpha\alpha} = (d_\alpha + d_{\alpha'})/2$. To compensate for strong depletion forces between two motors the repulsive potential between two beads in different motors has $\sigma_{MM} = d_C + \sigma$. Interactions between solvent particles and motor and filament beads are also described by repulsive LJ potentials with strength $\epsilon_{\alpha S}$ and cutoff distance $r_c = 2^{1/6}\sigma_{\alpha S}$, where $\sigma_{\alpha S} = (d_\alpha + d_S)/2$. When solvent particles interact with a motor or filament bead, they have effective diameter $d_S = 0.5\sigma$. All solvent particles have the same mass m, while the masses of the motor and filament beads are chosen to be $m_\alpha = \frac{4}{3}\pi(d_\alpha/2)^3 n_0 m$ so that they have the same mass density as the bulk solution. The time evolution of the entire system is simulated by hybrid molecular dynamics-multiparticle collision dynamics (MD-MPCD) [33].

Multiparticle collision dynamics combines effective multiparitcle collisions at discrete time intervals τ with streaming between two consecutive collisions. Such collisions are carried out by first sorting the particles into cubic cells ξ with linear size a. We use the momentum-conserving Anderson thermostat version of multiparticle collision dynamics [38]. The postcollision velocity of particle i in cell ξ is given by

$$\mathbf{v}_i' = \mathbf{V}_i + \mathbf{v}_i^{\mathrm{ran}} - \sum_{j \in \mathrm{cell}\xi} \mathbf{v}_j^{\mathrm{ran}}/N_\xi. \tag{A.1}$$

Here the components of $\mathbf{v}_i^{\mathrm{ran}}$ are Gaussian random numbers with zero mean and variance k_BT/m, N_ξ is the total number of solvent particles in the cell, and $\mathbf{V}_\xi$ is the center-of-mass velocity of these N_ξ particles. Grid shifting was employed to ensure Galilean invariance [39, 40]. In the streaming steps, the dynamics of all the species is governed by molecular dynamics under the potential functions mentioned above. The collisions among solvent particles are carried out using reactive multiparticle collision dynamics [36]. Reactions in the bulk phase takes place independently in each cell ξ at each MPC collision step. In the cell ξ, the reaction $B \to A$ occurs with probability $p_j^\xi(N_B^\xi) = 1 - e^{-a_2^\xi \tau}$, where N_B^ξ is the total number B particles in the cell ξ and $a_2^\xi = k_2 N_B^\xi$ with $k_2 = 0.01$ the bulk reaction rate.

The time evolution of the entire system is carried by using velocity-Verlet algorithm with a molecular dynamics time step, $\delta t = 0.01\, t_0$, and multiparticle collision time, $\tau = 0.5\, t_0$. The system temperature is $k_BT = 0.2\,\epsilon$. Interaction strengths among motor and filament beads are $\epsilon_{MF} = 0.1\,\epsilon$ and among motor beads $\epsilon_{MM} = \epsilon$. Solvent particles interact with filament beads with strength $\epsilon_{SF} = \epsilon$, and with motor beads through different strengths as described in sect. 2. For distinct-product simulations, the N bead in motor i and a product particle B_j produced by motor j have interaction strength $\epsilon_{N_iB_j}$. If $i = j$, then $\epsilon_{N_iB_j} = 0.1\,\epsilon$; otherwise $\epsilon_{N_iB_j} = \epsilon$. Note that there are no repulsive interactions among the beads in the same motor and in the filament. There are $N_S = 140\,700$ solvent particles in the system so that the solvent density is $n_0 \approx 9$. The multiparticle collision cell size is $a = \sigma$. Two neighboring beads in the motor or in the filament are connected by harmonic springs with the spring constant $k_s = 100\,\epsilon/\sigma^2$, and with equilibrium lengths $r_0^M = 1.5\,\sigma$ and $r_0^F = \sigma$. The bending stiffness of the filament is $k_b = 100\,\epsilon$. Results are reported in dimensionless units with mass m, length σ, energy ϵ, and time $t_0 = \sqrt{m\sigma^2/\epsilon}$.

Appendix B. Product number density field

The average number density field of B product particles, $n_B(\mathbf{r_S})$, in the vicinity of a motor attached to a filament is determined by measuring the product density field in a planar slice with normal perpendicular to the motor internuclear axis, $\hat{\mathbf{u}}$. We consider three orthogonal vectors: two in-plane vectors $\hat{\mathbf{n}}_1$ and $\hat{\mathbf{n}}_2$, and a vector $\hat{\mathbf{n}}_3 = \hat{\mathbf{n}}_1 \times \hat{\mathbf{n}}_2$ normal to the plane, and thus the density field can written in terms of the in-plane coordinates $n_B = n_B(n_1, n_2)$. The orientation vector $\hat{\mathbf{u}}$ is chosen to be $\hat{\mathbf{n}}_1$ and the normal vector $\hat{\mathbf{n}}_3$ should be chosen such that the plane is nearly parallel to the filament, *i.e.*, the plane intersects the filament bead at distant position. To find $\hat{\mathbf{n}}_3$, a vector $\hat{\mathbf{n}}_3'$,

$$\hat{\mathbf{n}}_3' = \frac{\mathbf{R}_L - (\mathbf{R}_L \cdot \hat{\mathbf{x}})\hat{\mathbf{x}}}{|\mathbf{R}_L - (\mathbf{R}_L \cdot \hat{\mathbf{x}})\hat{\mathbf{x}}|}, \tag{B.1}$$

is taken, which is in the radial direction around the x-axis (the filament axis), and the normal vector $\hat{\mathbf{n}}_3$ is then given by

$$\hat{\mathbf{n}}_3 = \frac{\hat{\mathbf{n}}_3' - (\hat{\mathbf{n}}_3' \cdot \hat{\mathbf{n}}_1)\hat{\mathbf{n}}_1}{|\hat{\mathbf{n}}_3' - (\hat{\mathbf{n}}_3' \cdot \hat{\mathbf{n}}_1)\hat{\mathbf{n}}_1|}. \tag{B.2}$$

The next step is to determine the position of B particles in the planar slice. By using the position of the L bead as the origin, the vector pointing from the origin to the B particle at $\mathbf{r}$ is $\mathbf{r}' = \mathbf{r} - \mathbf{R}_L$. The distance between the B particle and the plane is $d = |\mathbf{r}' \cdot \hat{n}_3|$, and only the B particles located in the slice are taken into account which means the condition $2|d| < 0.1$ must be satisfied, where the slice thickness is 0.1. The coordinates of the B particle projected on the plane can be computed by

$$\mathbf{r}_S = (\mathbf{r}' \cdot \hat{\mathbf{n}}_1)\hat{\mathbf{n}}_1 + (\mathbf{r}' \cdot \hat{\mathbf{n}}_2)\hat{\mathbf{n}}_2, \tag{B.3}$$

where the S denotes the in-plane vector. Thus, the density profile is computed by sorting the B particles into a 120×80 lattice of cells, each of which has linear size of 0.1, the same as the slice thickness, according to the in-plane coordinates $\mathbf{r}_S$. The average density in each lattice cell is given by the average over the ensemble of motors attached to the filament and over time.

References

1. M.E. Cates, J. Tailleur, EPL **101**, 20010 (2013).
2. S. Saha, R. Golestanian, S. Ramaswamy, Phys. Rev. E **89**, 062316 (2014).
3. T. Speck, A.M. Menzel, J. Bialké, H. Löwen, J. Chem. Phys. **142**, 224109 (2015).
4. S. Ramaswamy, Annu. Rev. Condens. Matter Phys. **1**, 323 (2010).
5. T. Vicsek, A. Zafeiris, Phys. Rep. **517**, 71 (2012).
6. W. Wang, W. Duan, S. Ahmed, T.E. Mallouk, A. Sen, Nano Today A **8**, 531 (2013).
7. M.C. Marchetti, J.F. Joanny, S. Ramaswamy, T.B. Liverpool, J. Prost, M. Rao, R.A. Simha, Rev. Mod. Phys. **85**, 1143 (2013).
8. J. Bialké, T. Speck, H. Löwen, J. Non-Cryst. Solids **407**, 367 (2015).
9. G.D. Magistris, D. Marenduzzo, Physica A **418**, 65 (2015).
10. V. Yadav, W. Duan, P.J. Butler, A. Sen, Annu. Rev. Biophys. **44**, 77 (2015).
11. J. Elgeti, R.G. Winkler, G. Gompper, Rep. Prog. Phys. **78**, 056691 (2015).
12. Andreas Zöttl, Holger Stark, arXiv:1601.06643 [cond-mat.soft].
13. B. Alberts, D. Bray, J. Lewis, M. Raff, K. Roberts, J.D. Watson, *Molecular Biology of the Cell*, 3rd edition (Garland Science, 2002).
14. R.A.L. Jones, *Soft Machines: Nanotechnology and Life* (Oxford University Press, Oxford, 2004).
15. B. Alberts, Cell **92**, 291 (1998).
16. R. Kapral, J. Chem. Phys. **138**, 020901 (2013).
17. I. Theurkauff, C. Cottin-Bizonne, J. Palacci, C. Ybert, L. Bocquet, Phys. Rev. Lett. **108**, 268303 (2012).
18. W. Gao, A. Pei, X. Feng, C. Hennessy, J. Wang, J. Am. Chem. Soc. **135**, 998 (2013).
19. M. Ibele, T.E. Mallouk, A. Sen, Angew. Chem. Int. Ed. **48**, 3308 (2009).
20. J. Palacci, S. Sacanna, A.P. Steinberg, D.J. Pine, P.M. Chaikin, Science **339**, 936 (2013).
21. I. Buttinoni, J. Bialké, F. Kümmel, H. Löwen, C. Bechinger, T. Speck, Phys. Rev. Lett. **110**, 238301 (2013).
22. H.-Y. Chen, K.-T. Leung, Phys. Rev. E **73**, 056107 (2006).
23. K.-T. Leung, H.-Y. Chen, Int. J. Mod. Phys. B **21**, 3954 (2007).
24. A. Zöttl, H. Stark, Phys. Rev. Lett. **112**, 118101 (2014).
25. M. Hennes, K. Wolff, H. Stark, Phys. Rev. Lett. **112**, 238104 (2014).
26. O. Pohl, H. Stark, Phys. Rev. Lett. **112**, 238303 (2014).
27. J.L. Anderson, Ann. Rev. Fluid Mech. **21**, 61 (1989).
28. R. Golestanian, T.B. Liverpool, A. Ajdari, Phys. Rev. Lett. **94**, 220801 (2005).
29. G. Rückner, R. Kapral, Phys. Rev. Lett. **98**, 150603 (2007).
30. M.-J. Huang, R. Kapral, J. Chem. Phys. **142**, 245102 (2015).
31. M.-J. Huang, R. Kapral, A.S. Mikhailov, H.-Y. Chen, J. Chem. Phys. **138**, 195101 (2013).
32. A. Malevanets, R. Kapral, J. Chem. Phys. **110**, 8605 (1999).
33. A. Malevanets, R. Kapral, J. Chem. Phys. **112**, 72609 (2000).
34. R. Kapral, Adv. Chem. Phys. **140**, 89 (2008).
35. G. Gompper, T. Ihle, D.M. Kroll, R.G. Winkler, Adv. Polym. Sci. **221**, 1 (2009).
36. K. Rohlf, S. Fraser, R. Kapral, Computs. Phys. Commun. **179**, 132 (2008).
37. C. Loken, D. Gruner, L. Groer, R. Peltier, N. Bunn, M. Craig, T. Henriques, J. Dempsey, C.-H. Yu, J. Chen, L.J. Dursi, J. Chong, S. Northrup, J. Pinto, N. Knecht, R. Van Zon, J. Phys.: Conf. Ser. **256**, 012026 (2010).
38. H. Noguchi, N. Kikuchi, G. Gompper, EPL **78**, 10005 (2007).
39. T. Ihle, D.M. Kroll, Phys. Rev. E **63**, 020201 (2001).
40. T. Ihle, D.M. Kroll, Phys. Rev. E **67**, 066705 (2003).